https://doi.org/10.5194/egusphere-2023-1813
Preprint. Discussion started: 14 August 2023

3D shear wave velocity imaging of the subsurface structure of granite rocks in the arid climate of Pan de Azúcar, Chile, revealed by Bayesian inversion of HVSR curves

Rahmantara Trichandi[1,2,*], Klaus Bauer[1], Trond Ryberg[1], Benjamin Heit[1], Jaime Araya Vargas[3], Friedhelm von Blanckenburg[1,4], Charlotte M. Krawczyk[1,2]

[1]GFZ German Research Centre for Geosciences, Telegrafenberg, 14473 Potsdam, Germany
[2]Technische Universität Berlin, Ernst-Reuter-Platz 1, 10587 Berlin, Germany
[3]Departamento de Geología, Universidad de Atacama, Copiapó, Chile
[4]Institute of Geological Sciences, Freie Universität Berlin, Berlin, Germany

Correspondence to: Rahmantara Trichandi (chandi@gfz-potsdam.de)

Abstract. Seismic methods are emerging as efficient tools for imaging the subsurface to investigate the weathering zone. The structure of the weathering zone can be identified by differing shear wave velocities as various weathering processes will alter the properties of rocks. Currently, 3D subsurface modelling of the weathering zone is gaining increasing importance as their results allow the identification of the weathering imprint in the subsurface not only from top to bottom but also in three dimensions. We investigated the 3D weathering structure of monzogranite bedrock near the Pan de Azúcar National Park (Atacama Desert, Northern Chile), where the weathering is weak due to the arid climate condition. We set up an array measurement that records seismic ambient noise, which we used to extract the horizontal-to-vertical spectral ratio (HVSR) curves. The curves were then used to invert for 1D shear wave velocity models, which we then used to compile a pseudo-3D model of the subsurface structure in our study area. To invert the 1D shear wave velocity model, we apply a trans-dimensional hierarchical Bayesian inversion scheme, allowing us to invert the HVSR curve with minimum prior information. The resulting 3D model allowed us to image the granite gradient from the surface down to ca. 50 meters depth and confirmed the presence of dikes of mafic composition intruding the granite. We identified three main zones of fractured granite, altered granite, and the granite bedrock in addition to the mafic dikes with relatively higher Vs. The fractured granite layer was identified with Vs of 1.4 km/s at 30 – 40 meter depth, while the granite bedrock was delineated with Vs of 2.5 km/s and a depth range between 10 and 50 meters depth. We compared the resulting subsurface structure to other sites in the Chilean coastal cordillera located in various climatic conditions and found that the weathering depth and structure at a given location depends on a complex interaction between surface processes such as precipitation rate, tectonic uplift and fracturing, and erosion. Moreover, these local geological features such as intrusion of mafic dikes can create significant spatial variations to the weathering structure and therefore emphasize the importance of 3D imaging of the weathering structure. The imaged structure of the subsurface in Pan de Azúcar provides the unique opportunity to image the heterogeneities of a rock preconditioned for weathering, but one that has never experienced extensive weathering given the absence of precipitation.

https://doi.org/10.5194/egusphere-2023-1813
Preprint. Discussion started: 14 August 2023

1. Introduction

Weathering can modify the mineralogy of rocks, resulting in petrophysical changes that can be detected with geophysical methods. Numerous geophysical imaging techniques have been successfully applied to characterize the weathering structure in granitic rocks, including the use of electrical resistivity tomography (Olona et al., 2010; Holbrook et al., 2014), Ground Penetrating Radar (GPR) (Dal Bo et al., 2019) and seismic tomography (Trichandi et al., 2022; Befus et al., 2011; Olona et al., 2010; Handoyo et al., 2022). These non-invasive techniques allow to estimate the weathering structure over wide extents and/or in areas of deep weathering, where probing using traditional techniques (e.g., soil pits) is logistically expensive or can be even unfeasible.

Seismic body wave tomography is one of the most frequently used methods in weathering zone studies (Befus et al., 2011; Flinchum et al., 2018; Olona et al., 2010; Trichandi et al., 2022). The seismic signals generated by sources such as hammer, weight drop, or vibroseis are recorded by an array of seismic receivers. Seismic P-wave velocity can be inferred by analysis and inversion of body waves' travel time. However, data acquisition of such body wave tomography experiments can be extensive. It requires the appropriate source and receiver array setup and restricts data acquisition in remote areas where heavy equipment transportation can be challenging. Moreover, active seismic experiments are often not permitted in conservation areas such as national parks, where the impact of the seismic source can disturb the surrounding ecosystems.

The Horizontal-to-Vertical Spectral Ratio (HVSR) technique is a passive seismic method that does not rely on active seismic sources. It has emerged as a viable alternative to active seismic methods for effectively imaging the sub-surface weathering zone. Applied initially for site characterization in seismic hazard assessment (Piña-Flores et al., 2020; Mahajan et al., 2012) and imaging of sedimentary basins (Cipta et al., 2018; Pastén et al., 2016; Koesuma et al., 2017; Pilz et al., 2010), the HVSR method has recently been utilized at smaller scales for investigating bedrock (Maghami et al., 2021; Moon et al., 2019; Nelson & McBride, 2019; Trichandi et al., 2023). This approach has gained popularity due to its simplicity, rapid data acquisition, and ease of placing measurement points. However, it is important to note that the inverse problem associated with the HVSR curve is highly non-linear and necessitates prior knowledge of the subsurface structure (Moon et al., 2019; Nelson & McBride, 2019; Pilz et al., 2010).

Utilizing a trans-dimensional and hierarchical Bayesian Markov chain Monte Carlo (McMC) approach solves the prior information requirement challenge in HVSR curve inversion. This approach is beneficial as it only requires minimal prior information about the sub-surface structure during the inversion process (Ryberg and Haberland, 2019; Trichandi et al., 2022). Moreover, the trans-dimensional approach allows for changes in dimensionality throughout the inversion, eliminating the need for prior constraints on determining the number of layers (Cipta et al., 2018; Bodin, 2010; Bodin et al., 2012). Consequently, this procedure reduces uncertainty levels and provides a robust, data-driven Vs (shear wave velocity) model that can be readily interpreted.

In this paper, we explored the shallow (< 50 m) subsurface structure of granite bedrock in the arid climate near the Pan de Azúcar National Park, which is one of the test sites of the "EarthShape (Earth Suraface Shaping by Biota)" project that cover

https://doi.org/10.5194/egusphere-2023-1813
Preprint. Discussion started: 14 August 2023

the Chilean climate gradient from dry to humid (Oeser et al., 2018; Oeser & von Blanckenburg, 2020). In this study, we apply the HVSR method combined with the Bayesian inversion approach to produce a 3D subsurface image of the weathering structure around an existing borehole (-26.302717° N, -70.457350° W). Then, we compare the results with previous studies conducted at the other EarthShape test sites to study further the effects of different climate and geological processes on the deep weathering of granite.

2. Study site and geological setting

The study was conducted at the outskirt of the Pan de Azúcar National Park, located in the Atacama Desert, approximately 200 km north of Copiapó, Chile (Figure 1A). The area is located in the arid part of the Coastal Cordillera featuring very low precipitation of ~10 mm/year and a mean annual temperature of 18.3 °C (Karger et al., 2017; Oeser et al., 2018). With such low precipitation, the vegetation in this area is minimal and is mainly sustained by the coastal fog coming in from the Pacific Ocean (Lehnert et al., 2018). A Ground Penetrating Radar (GPR) study in the Pan de Azúcar National Park managed to image the subsurface down to 2 meters depth, revealing an average soil thickness of 0.20 m (Dal Bo et al., 2019). Information from greater depth was not obtained due to the frequency limitation (Dal Bo et al., 2019).

The study area is in the Triassic Cerros del Vetado pluton (Figure 1B), comprising monzogranites and syenogranites (Godoy and Lara, 1998). Reported U-Pb ages for this pluton are in the range of 205-250 Ma (Berg and Baumann, 1985; Maksaev et al., 2014; Jara et al., 2021). Along its eastern margin, the Cerros del Vetado pluton is intruded by the Late Jurassic Las Ánimas pluton (Figure 1B), which has reported ages in the range of 150-160 Ma (Dallmeyer et al., 1996; Godoy and Lara, 1998; Jara et al., 2021). The Cerros del Vetado pluton is also intruded by a dense network of dikes with varying directions and compositions (Berg and Baumann, 1985; Acevedo, 2022), from which a swarm of NE-SW-oriented and dark-colored dikes of mafic (gabbroic to dioritic) composition is clearly observed in the field and crosses the study area (see dark-colored lines in Figure 1B and C). Dallmeyer et al. (1996) report a $^{40}Ar/^{39}Ar$ age of 129.2 ± 0.5 Ma for one of these dikes that outcrops 8 km south-west of the study area. In 2019, a drilling campaign was conducted to investigate the weathering structure by extracting drill cores to perform core analyses. The location of the borehole is shown in Figure 1D.

According to investigations of samples from the borehole, the bedrock at Pan de Azúcar is characterized by a high SiO2 (Ø 74 wt%), Na2O, and K2O content (> 7 wt%) and remarkably uniform major element concentrations. It comprises the major minerals of quartz, plagioclase, microcline, and biotite. The grain size distribution is relatively homogenous, with an average grain size around 0.5 cm. The granite has been hydrothermally overprinted to variable degrees. This alteration is strongest in the vicinity of large fractures. Televiewer data from the borehole revealed that fractures dip angles show a continuous range of dip angles between 20 and 80°. Fractures of shallower dip alternate with steeper dipping fractures throughout the entire core. Fractures are partly cemented with calcite, clay minerals, and Fe-oxides. Bedrock porosity is, with an average of around 1%, generally low, whereas the hydrothermally overprinted core material has a bulk porosity of exceeding 2.5%. Weathering mass balances using the refractory element niobium indicated zero weathering, as expected in arid climate. Mean soil

https://doi.org/10.5194/egusphere-2023-1813
Preprint. Discussion started: 14 August 2023

denudation rates measured at the drill site with in situ cosmogenic 10Be measured in quartz from surface soil is 7.1 ± 0.5 t km-2 yr-1 (n=3).

3. Data Acquisition

We conducted a passive seismic data acquisition in Pan de Azúcar in August 2022 in a 150 x 150 m area covering the borehole location (Figure 1C) with elevation varying between 710 – 750 meters. The investigated area extends from gently sloping bedrock in the southeast into a colluvial valley fill consisting of sandy gravel in the northwest. The distance between measurement points was set to be 10 meters apart, resulting in 225 measurement points. Initially, a larger area was planned for the data acquisition. However, the hard rock surface and steep topography made deploying the geophones southeast of the borehole location impossible. The ambient noise data was acquired by the subsequent deployment of 15 3-components (3-C) geophones with 4.5 Hz Eigenfrequency (PE-6/B by SENSOR Nederland). Since we expected a shallow weathering structure, the 4.5 Hz Eigenfrequency is deemed to be sufficient to cover the desired depth range. The geophones were planted into the ground and were connected to a CUBE data logger (DATA-CUBE³ Type 1 with internal GPS – by DiGOS), which records the seismic vibrations detected by the geophones. We simultaneously deployed 15 geophones along a northwest – southeast direction line and recorded the ambient seismic noise for 1 hour for each measurement point. To cover the whole area with 225 measurement points, we required four days of fieldwork, including the array setup.

4. Methodology

To image the subsurface using the Horizontal-to-Vertical Spectral Ratio (HVSR) method, we first need to process the recorded 3-component noise data and extract the HVSR curve. When extracting the curves, we followed the statistical approach described by Cox et. al. (2021). To guarantee sufficient data quality, we excluded the curves that did not satisfy the SESAME Guideline for site characterization (SESAME, 2004). Then, we inverted each curve using a trans-dimensional, hierarchical Bayesian inversion approach to get a 1D Vs profile from each measurement point. We then used the multiple 1D profiles to produce a pseudo-3D Vs model of the subsurface by smoothing and interpolation.

4.1. HVSR curve extraction

Prior to the HVSR curve extraction process, we applied instrumental correction and a 1.0 to 150 Hz bandpass filter to the three components' raw data (vertical, east-west, and north-south). We used the 60 minutes of ambient noise for each point, as shown by the example in Figure 2A – C. The time-series data were then transformed into a frequency domain by applying a straightforward Fourier transform (Figure 2D – F). To improve the quality and stability of our HVSR curve, we followed the statistical approach of HVSR curve extraction described by Cox et. al. (2021). We divided the time series data into 60 seconds

https://doi.org/10.5194/egusphere-2023-1813
Preprint. Discussion started: 14 August 2023

time windows and rejected time windows that exceeded a statistical threshold of peak frequency and variance. Ultimately, we obtained the final HVSR curve and the corresponding standard deviation shown in Figure 2G.

After extractions of the HVSR curve from all the observation points, we checked for the HVSR curve's consistency. Color plots of the HVSR curve in Figure 3A reveal mainly two frequency ranges with the peak frequency: below 30 Hz and around 100 Hz. Since the study is more focused on the boundary between the bedrock and its overlaying weathering structure, the higher frequency data will later be discarded as the HVSR curve peak around 100 Hz is often associated with the boundary between soil and saprolite (Nelson and McBride, 2019). The HVSR curve with high uncertainties will also later be discarded. An average of all the HVSR curves is shown in Figure 3B, where it is possible to observe various frequency peaks in the frequency range lower than 10 Hz, which could be related to the varying bedrock depth.

4.2. HVSR curve inversion

The substantial non-uniqueness inherent in the HVSR curve modelling introduces a highly non-linear inverse problem. Various approaches have been employed to address this challenge, including the implementation of a least-square approach (Arai and Tokimatsu, 2004), fixing the number of layers (Fäh et al., 2003; Parolai et al., 2005; Hobiger et al., 2013; Wathelet et al., 2004), and fixing the bedrock velocity (Parolai et al., 2005). These approaches tried to simplify the inverse problem by incorporating prior information about the true model into the inversion process. For instance, it is often difficult to determine the expected number of layers without preliminary subsurface investigations in the context of investigating weathering zones. As for fixing the bedrock velocity, although previous research on similar bedrock formations can provide some prior knowledge about the velocity, it is common for bedrock velocities to vary between different sites (Trichandi et al., 2023, 2022). Furthermore, reliably fixing the bedrock velocity would necessitate accurate bedrock P- and S-wave velocity information.

We utilized a trans-dimensional hierarchical Bayesian Markov Chain Monte Carlo inversion scheme instead of simplifying the inverse problem by putting constraints and feeding prior information to the inversion parameters. The main advantage of using this inversion scheme is that we require only minimum prior information about the real model (Ryberg and Haberland, 2019; Trichandi et al., 2022). Furthermore, with the trans-dimensional approach, we do not have to define a fixed number of layers for our model, as the number of layers will be determined during the inversion process based on the data noise level. For the inversion workflow, we followed the scheme described by Bodin (2010), which had also been applied to the HVSR curve inversion (Cipta et al., 2018; Trichandi et al., 2023).

For the parameterization of the inversion, we defined a wide range of values for each parameter. The Vs value was determined to be between 0.1 and 5.0 km/s to accommodate the possible existence of very loose material, such as soil with low velocity or even intruding solid rocks layer with very high velocity. The advantage of using a relatively large model space is also to allow the inversion scheme to explore the whole model space and not be trapped in a local minimum. For the number of layers, we also enabled the inversion to explore models with a number of layers between 2 and 20 layers (including half space).

Forward calculation of the HVSR curve also requires an explicit definition of the number of layers. We accommodated the inversion to explore both simple and complex layered models by performing a trans-dimensional inversion approach. While

https://doi.org/10.5194/egusphere-2023-1813
Preprint. Discussion started: 14 August 2023

the conventional approach often subdivides weathering layers into three or four layers, we allow the inversion to explore a simple two-layered model. This simple layered model accommodates situations where only fractured bedrock and bedrock layers are present, particularly in areas with a relatively low degree of weathering. Furthermore, this simplified model is beneficial for incorporating data with high uncertainty. Conversely, we also allowed a maximum of 20 layers to account for the possibility of highly intricate sub-surface layering, acknowledging the potential complexity that may be present in certain areas.

The subsequent parameters to be determined are Vp and density. Previous studies have demonstrated that these parameters exhibit relatively low sensitivity to HVSR curve modeling and can be considered unknown nuisances during the inversion process (Cipta et al., 2018). However, for completeness, we also established uniform ranges for Vp, ranging from 0.3 to 8.0 km/s, and for density, ranging from 1.5 to 3.0 g/cm3. It is also important to note that we did not invert the density value in our inversion and used the inverted Vp value for the density approximation.

We performed the inversion for each data point on 24 parallel Markov chains with 100,000 iterations per chain. Each chain starts by drawing a random initial model (m_0) from the given prior information. The initial model is then used to model a HVSR curve ($dcal_0$) using the GEOPSY forward modelling package (Wathelet et al., 2020). The forward calculation tool employed a model representing the sub-surface as a series of homogeneous layers extending into a half-space. We used a 1D Voronoi cell approach of constant velocity layer when constructing the layered model. Then for every iteration, one of the following perturbations was performed:

- Perturb the data noise (σ) value according to the proposal distribution.
- Perturb the Voronoi cell location of a random cell according to the proposal distribution. Changes in the Voronoi cell location will affect the layer's thickness of the input model.
- Perturb the Vs value of a random cell according to the proposal distribution.
- According to the proposal distribution, perturb a random cell's Vp/Vs value and calculate Vp accordingly for the input model.
- Delete one random cell.
- Add one random cell based on the prior information provided by the chain.

The perturbation process generates a new model (m_1), from which we calculate the corresponding HVSR curve ($dcal_1$). Subsequently, we determine the acceptance probability for transitioning from the initial model (m_0) to the new model (m_1) based on the observed data (dobs), the calculated HVSR curve of the initial model ($dcal_0$), and the calculated HVSR curve of the new model ($dcal_1$). We randomly decide whether to accept the transition from m0 to m1 using this acceptance probability. If the transition is accepted, m_1 replaces m_0, and we proceed to the next iteration. However, if the transition is not accepted, we retain m_0 and move on to the next iteration. This process is repeated until the specified number of iterations is reached. The final model for each station is obtained by averaging all the accepted models from the 24 Markov chains that were executed.

https://doi.org/10.5194/egusphere-2023-1813
Preprint. Discussion started: 14 August 2023

5. Results

We divided our results into two main parts: (1) results from the HVSR curve and the subsequent (2) pseudo-3D Vs model. Even before performing the HVSR curve inversion, the HVSR curve already brings an insight into the weathering zone depth as the peak frequency from the HVSR curve is often linked to the top of the bedrock depth (Nelson and McBride, 2019; Nagamani et al., 2020; Stannard et al., 2019).

5.1. HVSR curve frequency profile

After extracting the HVSR curves, we can determine the peak/resonance frequency (f_0) of each HVSR curve and produce the peak frequency and apparent fresh bedrock depth map (Figure 4A and B). The peak frequency map in Figure 4A can be created by plotting each measurement point's peak frequency. The high frequency in Figure 4A is related to a shallower interface between the regolith and bedrock, while low frequency means a deeper interface. Using the peak frequency map in Figure 4A, we can also produce an apparent bedrock depth map using an approximation of the following:

$$D = \frac{1}{4f^0}\, V_s$$

With this approximation, we can quickly estimate the fresh bedrock depth across the study area. Figure 4B shows the apparent bedrock depth obtained using equation 1, assuming a Vs of 1.5 km/s for overlaying layer. This value is reasonable as we expect the bedrock to be overlain by a fractured bedrock which can have a Vs up to 1.5 km/s (Trichandi et al., 2022, 2023).

From the peak frequency and apparent fresh bedrock depth map, we can already see an interesting feature in our study area. The most distinctive feature is the two southwest–northeast stripes of high peak frequencies – related to the shallow interface to the bedrock layer. However, certain precautions have to be taken when interpreting this apparent fresh bedrock depth map, especially as the apparent fresh bedrock depth formula assumes a homogenous value of the layer velocity and a sharp Vs contrast between the layers. Nevertheless, the peak frequency and apparent bedrock depth map still serve as a good indicator of potential contrasting subsurface structure. In our case study area, the peak frequency is likely related to the interface between fractured bedrock and bedrock unit, as we do not find any indication of a saprolite unit in the study area.

5.2. S-wave velocity depth profile

We present an example of the 1D S-wave velocity profile result of a data point located 1 meter away from the borehole (Figure 5) to demonstrate the robustness of the Bayesian inversion routine. The modelled HVSR curve matched well with the observed curve and is well within the modelled standard deviation (Figure 5A). Figure 5B shows how the inversion routine explored the Vs model space within the widely defined Vs corridor. In the end, the 1D Vs model was derived from the average of all the Vs models, as shown in Figure 5B. Here we can see that at the borehole location, the Vs down to 28 – 30 meters depth are relatively constant, followed by a slight increase from 30 to 40 meters depth. Starting from a 40-meter depth, a slight increase in Vs value can be observed until 55 meters depth. Below this, the increase in Vs is not as steep, but we can still see an increase until around 40 meters deep, where we start losing the resolution due to half-space models.

https://doi.org/10.5194/egusphere-2023-1813
Preprint. Discussion started: 14 August 2023

Since we utilize Voronoi cells in the model parameterization, the Bayesian inversion also produces an interface probability model function (Figure 5C). This function shows the probability of a likely interface between the layers based on the models produced from all the inversion chains. The interface probability offers four possible interfaces in our data around 15, 28, 48, and 60 meters in depth. These interfaces coincide with some of the interpreted interfaces from drill core interpretation in Figure 5D (Stroncik & von Blanckenburg, 2022).

We compiled the resulting 1D Vs model and interpolated them to create a volumetric cube of Vs value. A series of depth slices from 10 – 50 meters depth is presented in Figure 6, where we can see a similar NE – SW feature as in Figure 4. This feature can be observed from 10 meters depth and is getting stronger at 20 meters. At smaller depths, the velocity is relatively low (< 1.50 km/s) except around the previously mentioned NE-SW features, with the lowest velocity of around 1.00 km/s. These low-velocity features remain until 30 meters depth (Figure 6C) where the high velocity starts to take over the low-velocity values around the area. Then at 40- and 50-meters depth, the remaining low-velocity area is located northwest of the borehole.

We also plot a horizontal depth slice of 28-meter depth / 693 masl (Figure 7A) following the end of the altered granite layer interpreted in the borehole core interpretation (Figure 5D), and to further investigate the interesting NE-SW features, we also create a vertical slice of our data perpendicular to the NE-SW features and going through the borehole location (Figure 7B). The vertical slice shows varying Vs between 1.0 – 3.0 km/s. Horizontally, we do not see so many variations except in the western part of the profile, where we can see a relatively lower velocity layer right before the slope. Vertically, we can divide the profile into three main Vs layers. The first section is the layer with Vs < 1.40 km/s which covers down to 15 meters in depth. This section is relatively parallel to the surface topography. Then, we have the section with Vs between 1.40 and 2.40 km/s which covers a depth between 15 and 30 meters and shows more horizontal variations compared to its overlaying layer. Finally, the section with Vs > 2.40 km/s starts around 30 meters in depth near the dashed line reference in Figure 7B.

In addition to the vertical slice across the borehole, we present a vertical section north of the borehole location (Figure 8). Similar to the profile in Figure 7B, the Vs value in this profile also ranges between 1.0 and 3.0 km/s. However, instead of the relatively parallel homogenous horizontal variations in Figure 7B, in this profile, we can see an interesting near-vertical structure of high-velocity ca. 10 meters below the surface (Figure 8B).

6. Discussion

Using the HVSR method combined with the hierarchical Bayesian McMC inversion approach, we managed to image the 3D Vs velocity structure in the arid study site of Pan de Azúcar. We interpret and discuss possible weathering zone structures in the study area using the velocity model. In summary, we found four main structures in the study area: granite bedrock, fractured granite, basaltic intrusion, and hydrothermally altered granite. In addition to the identified structures, we also discuss different controlling processes that could explain the dynamics and formation of the weathering structure in the study area, including the effects of topography. Finally, we compared the structure in Pan de Azúcar to the other EarthShape sites in different climate conditions.

https://doi.org/10.5194/egusphere-2023-1813
Preprint. Discussion started: 14 August 2023

6.1. Granite bedrock

Various Vs values had been used to delineate the upper boundary of physically and chemically unweathered intact granite bedrock formation. Previous studies conducted in similar granitic environments have suggested that a Vs value of 2.0 km/s is an appropriate threshold between the granite bedrock and the overlying layer (Liu et al., 2022; Handoyo et al., 2022). Within the context of the Earthshape project, another geophysical investigation conducted in a site with a Mediterranean climate (La Campana National Park, see location in Figure 1A) has indicated that we can utilize a Vs value of 2.3 km/s to identify the upper limit of the bedrock layer (Trichandi et al., 2023). In a site with a semi-arid climate (Santa Gracia National Park, see location in Figure 1A), another study revealed that a Vs value of 2.5 km/s is appropriate for defining the upper boundary of the bedrock interface (Trichandi et al., 2022). We can attribute the selection of different Vs values to determine the bedrock's upper limit to either variation in lithological composition or the impact of distinct climatic conditions. Nevertheless, given the similarity in climate, we opted to employ a Vs value of 2.5 km/s to establish the upper boundary of the bedrock in our study area.

Based on the Vs value across the area in Figure 6, we can see that the 2.5 km/s Vs value started at different depth ranges. In Figure 6A and B, we can see that even at shallow depths of 10 and 20 meters, Vs is already at 2.5 km/s. However, we believe that the NE-SE trending high-Vs zones in the middle of the study area are related to dikes of mafic composition, which we will discuss in section 6.3. Therefore, we believe that the physically intact bedrock starts from 30 meters deep at the shallowest, as shown by the high Vs value in the south-western part of the area shown in Figure 6C. This high Vs value is then becoming more prominent in the 40- and 50-meter depth slice (Figure 6D and E), where we can see that the high Vs value is spreading to the north-east direction. Based on this 3-dimensional observation, we can already see that instead of a uniform bedrock depth, as shown in Figure 7B, the top of the bedrock depth is more variable in the different directions. An intact bedrock depth between 30 to 50-meter depth agrees with other previous studies that found intact bedrock depth in an arid and semi-arid area to be between 30 to 70 meters depth (Stierman and Healy, 1984; Vázquez et al., 2016; Trichandi et al., 2022).

6.2. Fractured granite

The presence of fractures in the bedrock leads to a systematic decrease in the Vs values. Previous studies have shown that Vs values between 1.3 – 1.4 km/s can be used to identify the top of the fractured bedrock layer (Trichandi et al., 2022, 2023). Based on the horizontal depth slice of the Vs model (Figure 6), we can already find Vs > 1.3 km/s even at 10 meters depth (Figure 6A) even when we exclude the NE-SW high-velocity features. The low velocity areas are of Vs < 1.3 km/s can be attributed to either fractured granite or colluvial valley fill. Field observations did observe the existence of colluvial valley between the two hills, but the extent of this valley fills was not further investigated. Since colluvial valley will usually shows lower Vs values (< 1.0 km/s) (Handoyo et al., 2022), we opted to attribute this unit as granite rocks with significant amount of fractures within. However, it is also possible that the thickness of this colluvial valley is well below the vertical resolution of our HVSR method and therefore we do not observe its low Vs signature. Nevertheless, the vertical extent of the identified

https://doi.org/10.5194/egusphere-2023-1813
Preprint. Discussion started: 14 August 2023

fractured bedrock layer seems to vary significantly across the area: while west of the borehole Vs >2 km/s are reached at depths shallower than 20 m (blueish zones in Figure 6C), in the northern part of the area Vs <1.3 km/s is observed up to 40 m depth (brownish colors in Figure 6D). This variation across the study area showcases the importance of 3D mapping in weathering front study, as it is easy to conclude a relatively uniform thickness of the fractured granite layer if we only consider a 2D profile across the borehole (Figure 7B).

Several processes can explain the fracturing of bedrock in our study area. Firstly, we can hypothesize that the fractures were formed during the cooling process of the plutonic rocks (Ellis and Blenkinsop, 2019). Should this be the case, fractured bedrock ßpö.in our study area was likely to date back to the emplacement of the Cerros del Vetado, which took place ca. 250-205 Ma. This emplacement likely happened in a depth range of 4 – 7 km (as most geobarometry studies of plutonic rocks of the Coastal Cordillera and Precordillera of northern Chile, e.g., Dallmeyer et al., 1996; Dahlström et al., 2022). Another possible explanation for the formation of this fractured granite layer is the process of lithostatic decompression, occurring at shallow depths due to the subduction-induced uplift and erosion of the entire coastal region. Considering that current denudation rates from cosmogenic nuclides are only 7.1 t/m^2/yr which corresponds to about 2.7 m/million years the fracturing would have taken place within the past several million years.

6.3. Mafic dikes

The Vs model consistently shows two NE-SW oriented zones of relatively higher Vs visible from 10 to 50 m depth (Figure 6). We interpret that these features are related to the Early Cretaceous NE-SW mafic dikes, which crop out around the study area and intrude on the Triassic Cerros del Vetado pluton (Figure 1B, D, and E). This hypothesis can explain the higher Vs values as the gabbro and diorite values are higher than granite (e.g., Christensen, 1996). The quasi-linear distribution of outcrops of these dikes in the study area (even when crossing small ridges, see Figure 1B) suggests that they have high-angle dips, consistent with the vertical shape of high Vs zones (Figure 8B).

Hypothetically, we can also ask if the mafic dikes intrusion could be the features which create the fractured granite unit. However, it is unlikely (and difficult to proof) that the current fractured granite layer was already present when the dikes emplaced (130 Ma), and that the fractured granite layer has been there over such a long time. According to thermochronological studies in the Coastal Cordillera of northern Chile (e.g., Juez-Larré et al., 2010; Rodríguez et al., 2018), there have been at least two significant exhumation events during the Cretaceous and the Eocene. If there was a shallow fractured granite layer during the emplacement of dikes ca. 130 Ma, such fractured granite layer likely was eroded after some of those exhumation events.

Based on the Vs model in Figure 8B, we create a conceptual lithology model in our cross-section where the dike feature is prominent (Figure 8C). From the bottom, we have the granite bedrock which were intruded by two mafic dikes. Then from ca. 30 meters depth to the surface, we have an overlying altered and fractured granite. The mafic dikes in our deployment area also do not seem to intrude up to the surface as we did not find any exposed dike in the middle of the profile during the data acquisition. This is also supported by the high Vs value that does not reach to the surface. Another possible explanation as to

https://doi.org/10.5194/egusphere-2023-1813
Preprint. Discussion started: 14 August 2023

why we did not find surface manifestation of the dike could be because of the colluvial fill which covers the middle area of our survey area. Nevertheless, based on this result and findings, we demonstrated the capability of HVSR method to identify a higher Vs structure in the subsurface even with minimal prior information.

6.4. Altered granite

Chronologically, the Cerros del Vetado pluton emplacement took place 250-205 Ma and likely in a depth range of 4-7km (as most geobarometry studies of plutonic rocks of the Coastal Cordillera and Precordillera of northern Chile, e.g., Dallmeyer et al., 1996; Dahlström et al., 2022). Then, the Las Ánimas pluton emplacement took place 160-150 Ma. This later emplacement might have induced hydrothermal alteration in the Cerros del Vetado pluton unit, as identified in the borehole. However, the emplacement of mafic dikes into the Cerros del Vetado pluton granites can also carry heat and possible fluids to enable hydrothermal alteration. The mafic dikes intruded the Cerros del Vetado pluton ca. 130 Ma (i.e., almost 100 Ma after Cerros del Vetado emplacement).

6.5. Controlling aspects of weathering structure

Based on the lithology identified in the study area, we summarised several significant controlling aspects that can affect the weathering structure. The first important aspect which could induce a particular weathering structure is the existence of fractures. Previous studies have shown fractures' importance in facilitating weathering processes (Trichandi et al., 2022; Brantley et al., 2017; Lodes et al., 2023). Across our study area, we identified fractured bedrock units that were likely formed due to tectonic stress or lithostatic decompression. The fracturing of the bedrock can be considered to preceed the first chemical weathering processes. The fractures, when connected, can act as pathways for fluid or other weathering agents and enable subsurface weathering. However, our study site in Pan de Azúcar provides an excellent observation of conditions preceeding chemical weathering. There, while bedrock has been physically changed into fractured bedrock, we see the conditions that in most locations on Earth would enable further physical, chemical, or biologically induced weathering. These, however, were absent in Pan de Azúcar given the absence of water and vegetation.

In addition to the availability of fractures due to preconditioning of the bedrock, the existence of geological structures also plays a significant role in shaping the weathering structure in our study site. A Previous study in the Santa Gracia Earthshape site shows how a possible fault could play an important role by allowing deeper weathering and providing fluid infiltration pathways (Trichandi et al., 2022). In Pan de Azúcar, the younger mafic dike intrusion could trigger fracturing, enabling hydrothermal alteration of the surrounding rocks. These findings emphasize the importance of looking at weathering structure not only as a 1D top–down interaction but also as a 3D interplay with the surrounding geological features.

Finally, climate effects in forms of precipitation also highly affect the weathering structure, especially in the near-surface. While our study area shows exposed fractured granite to the surface, the almost absence of precipitation restricts the surface's weathering process, which in return does turn the fractured bedrock into saprolite. While it is yet to be seen whether fog covers

https://doi.org/10.5194/egusphere-2023-1813
Preprint. Discussion started: 14 August 2023

coming in from the Pacific Ocean can affect the weathering structure, our Vs model indicates the absence of saprolite as we do not encounter a very low Vs value (typically below 0.8 km/s for saprolite).

6.6. Weathering depth and climate gradient

Our studies across the Chilean climate gradient show differing weathering structures. In the semi-arid climate of Santa Gracia, evidence from a borehole (Krone et al., 2021) and seismic imaging revealed a weathering front that reaches down to 30 meters in depth (Trichandi et al., 2022). Further studies in the Mediterranean climate of La Campana show a deepening of the weathering front down to around 60 meters depth (Trichandi et al., 2023). Based on these two sites, we can see the trend of weathering front deepening with increased precipitation as we go from dry climate in Santa Gracia to a more humid climate in La Campana.

However, at Pan de Azúcar, based on the Vs model, we can observe already a significant reduction of Vs on the surface (ca. 1,0 km/s) compared to the typical value of granite Vs (2.0 – 2.5 km/s). These reductions are likely to be related to the differing physical properties of the rocks due caused by physical processes which results in a fractured bedrock unit. The Vs data from Pan de Azúcar shows a deep, fractured bedrock zone down from very shallow depths to 30 meters depth, similar to the fractured bedrock depth in the Santa Gracia site. The absence of low Vs values (< 0.8 km/s) confirms that the fractured granite in Pan de Azucar did not experience significant weathering. This is in contrast to the weathering structure in Santa Gracia, where we can find low Vs values (< 0.8 km/s) typical of the Saprolite layer down to ca 8 meters depth (Trichandi et al., 2022). This shows that even when both sites have similar depth extent of the fractured bedrock as the preconditioning to enable weathering processes, the climate condition in Pan de Azúcar does not satisfy the condition to trigger extensive weathering of the fractured bedrock to saprolite. Therefore, when investigating the weathering structure, it is crucial to consider not only the depth of the weathering structure but also the intensity of the weathering, especially related to chemical processes.

7. Conclusion and outlook

The presented study showcases the importance of imaging the weathering zone, not only in 2D but also in a 3D point of view. Applying the HVSR method with the Bayesian inversion scheme provides a straightforward technique for 3D imaging of the weathering structure. The passive seismic nature of the HVSR method also enables data acquisition where usage of an active seismic source is restricted or even prohibited. The resulting 3D model also revealed dike features which we will not find if we only do a 2D imaging of the subsurface.

Based on the Vs model, we identified fractured and altered granite in Pan de Azúcar to reach 30 – 40 meters deep. We found no Vs signature of a saprolite layer that is indeed absent in Pan de Azúcar due to the arid climate. Mafic dike structures were identified at depth. Comparing the results of Pan de Azúcar (arid climate) with Santa Gracia (semi-arid) and La Campana (Mediterranean) EarthShape sites, we interpret that the depth and structure of weathering zone is a result of the complex interplay between fluid infiltration, the presence of interconnected pathways allowing fluid to migrate to great depth, and the

https://doi.org/10.5194/egusphere-2023-1813
Preprint. Discussion started: 14 August 2023

mineralogy of the bedrock before being exposed to surficial weathering. The imaged structure of the subsurface in Pan de Azúcar is unique in the sense that it shows a rock preconditioned for weathering, but one that has never experienced any extensive weathering given the absence of precipitation.

This study also further emphasizes the vital role of geophysical methods in imaging the weathering zone. This work shows that the employed seismic method helped differentiate geological features with distinctive weathering conditions (e.g., mafic dikes and the granites) that can be further investigated using a method with high resolution (e.g., borehole). This study also shows the importance of imaging the weathering zone in 3D, as the structures of weathering zone can exhibit significant variations in the horizontal direction.

8. Data availability

The data that support the findings will be available in the GFZ Data Repository following an embargo to allow for doctoral publication of research findings.

9. Author contributions

RT, KB, and CK planned the campaign; RT and BH performed the measurements; RT, KB, and TR analyzed the data; RT wrote the manuscript draft; KB, TR, BH, JAV, FVB and CK reviewed and edited the manuscript.

10. Competing interest

The authors declare that they have no conflict of interest.

11. Acknowledgement

We acknowledge support from the German Science Foundation (DFG) priority research program SPP-1803 ‘EarthShape: Earth Surface Shaping by Biota’ (Grant number KR 2073/5-1). Instruments for data acquisition were supported by the Geophysical Instrumental Pool Potsdam – GIPP (Grant number GIPP-201924). This work was also supported by EarthShape Coordination (EH 329/17-2, BL562/20-1). The authors are very thankful to K. Übernickel for her support in planning and performing the drilling campaign and downhole logging.

References

Acevedo, J.: Análisis petrológico/mineralógico y estructural del Plutón Cerros del Vetado, comuna de Chañaral, región de Atacama., Universidad de Atacama., 2022.

https://doi.org/10.5194/egusphere-2023-1813
Preprint. Discussion started: 14 August 2023

Arai, H. and Tokimatsu, K.: S-Wave Velocity Profiling by Inversion of Microtremor H/V Spectrum, Bulletin of the Seismological Society of America, 53–63 pp., 2004.

Befus, K. M. M., Sheehan, A. F. F., Leopold, M., Anderson, S. P. P., and Anderson, R. S. S.: Seismic Constraints on Critical Zone Architecture, Boulder Creek Watershed, Front Range, Colorado, Vadose Zo. J., 10, 915, https://doi.org/10.2136/vzj2010.0108, 2011.

Berg, K. and Baumann, A.: Plutonic and metasedimentary rocks from the Coastal Range of northern Chile: RbSr and UPb isotopic systematics, Earth Planet. Sci. Lett., 75, 101–115, https://doi.org/10.1016/0012-821X(85)90093-7, 1985.

Bodin, T.: Transdimensional Approaches to Geophysical Inverse Problems, PhD thesis, 243, https://doi.org/10.1021/jo00151a027, 2010.

Bodin, T., Sambridge, M., Tkalćić, H., Arroucau, P., Gallagher, K., and Rawlinson, N.: Transdimensional inversion of receiver functions and surface wave dispersion, J. Geophys. Res. Solid Earth, 117, 1–24, https://doi.org/10.1029/2011JB008560, 2012.

Brantley, S. L., Lebedeva, M. I., Balashov, V. N., Singha, K., Sullivan, P. L., and Stinchcomb, G.: Toward a conceptual model relating chemical reaction fronts to water flow paths in hills, Geomorphology, 277, 100–117, https://doi.org/10.1016/j.geomorph.2016.09.027, 2017.

Christensen, N. I.: Poisson's ratio and crustal seismology, J. Geophys. Res. Solid Earth, 101, 3139–3156, https://doi.org/10.1029/95JB03446, 1996.

Cipta, A., Cummins, P., Dettmer, J., Saygin, E., Irsyam, M., Rudyanto, A., and Murjaya, J.: Seismic velocity structure of the Jakarta Basin, Indonesia, using trans-dimensional Bayesian inversion of horizontal-to-vertical spectral ratios, Geophys. J. Int., 215, 431–449, https://doi.org/10.1093/gji/ggy289, 2018.

Dahlström, S. I. R., Cooper, F. J., Blundy, J., Tapster, S., Yáñez, J. C., and Evenstar, L. A.: Pluton Exhumation in the Precordillera of Northern Chile (17.8°–24.2°S): Implications for the Formation, Enrichment, and Preservation of Porphyry Copper Deposits, Econ. Geol., 117, 1043–1071, https://doi.org/10.5382/econgeo.4912, 2022.

Dal Bo, I., Klotzsche, A., Schaller, M., Ehlers, T. A., Kaufmann, M. S., Fuentes Espoz, J. P., Vereecken, H., and van der Kruk, J.: Geophysical imaging of regolith in landscapes along a climate and vegetation gradient in the Chilean coastal cordillera, Catena, 180, 146–159, https://doi.org/10.1016/j.catena.2019.04.023, 2019.

Dallmeyer, R. D., Brown, M., Grocott, J., Taylor, G. K., and Treloar, P. J.: Mesozoic Magmatic and Tectonic Events within the Andean Plate Boundary Zone, 26°-27°30'S, North Chile: Constraints from 40 Ar/ 39 Ar Mineral Ages, J. Geol., 104, 19–40, https://doi.org/10.1086/629799, 1996.

Ellis, J. F. and Blenkinsop, T.: Analogue modelling of fracturing in cooling plutonic bodies, Tectonophysics, 766, 14–19, https://doi.org/10.1016/j.tecto.2019.05.019, 2019.

Fäh, D., Kind, F., and Giardini, D.: Inversion of local S-wave velocity structures from average H/V ratios, and their use for the estimation of site-effects, J. Seismol., 7, 449–467, https://doi.org/10.1023/B:JOSE.0000005712.86058.42, 2003.

Flinchum, B. A., Steven Holbrook, W., Rempe, D., Moon, S., Riebe, C. S., Carr, B. J., Hayes, J. L., Clair, J. S., and Peters, M. P.: Critical zone structure under a granite ridge inferred from drilling and three-dimensional seismic refraction data, J. Geophys.

https://doi.org/10.5194/egusphere-2023-1813
Preprint. Discussion started: 14 August 2023

Res. Earth Surf., 123, 1317–1343, https://doi.org/10.1029/2017JF004280, 2018.

Godoy, E. and Lara, L.: Hojas Chañaral y Diego de Almagro, Región de Atacama, Servicio Nacional de Geología y Minería, Mapas Geológicos No. 5-6, 1 mapa escala 1:100.000, Santiago, 1998.

Handoyo, H., Defelipe, I., Martín-Banda, R., García-Mayordomo, J., Martí, D., Martínez-Díaz, J. J., Insua-Arévalo, J. M., Teixidó, T., Alcalde, J., Palomeras, I., and Carbonell, R.: Characterization of the shallow subsurface structure across the Carrascoy Fault System (SE Iberian Peninsula) using P-wave tomography and Multichannel Analysis of Surface Waves, Geol. Acta, 20, 1–19, https://doi.org/10.1344/GeologicaActayear.volume.manuscript, 2022.

Hobiger, M., Cornou, C., Wathelet, M., Di Giulio, G., Knapmeyer-Endrun, B., Renalier, F., Bard, P. Y., Savvaidis, A., Hailemikael, S., Le Bihan, N., Ohrnberger, M., and Theodoulidis, N.: Ground structure imaging by inversions of Rayleigh wave ellipticity: Sensitivity analysis and application to European strong-motion sites, Geophys. J. Int., 192, 207–229, https://doi.org/10.1093/gji/ggs005, 2013.

Holbrook, W. S., Riebe, C. S., Elwaseif, M., Hayes, J. L., Basler-Reeder, K., Harry, D. L., Malazian, A., Dosseto, A., Hartsough, P. C., and Hopmans, J. W.: Geophysical constraints on deep weathering and water storage potential in the Southern Sierra Critical Zone Observatory, Earth Surf. Process. Landforms, 39, 366–380, https://doi.org/10.1002/esp.3502, 2014.

Jara, J. J., Barra, F., Reich, M., Morata, D., Leisen, M., and Romero, R.: Geochronology and petrogenesis of intrusive rocks in the Coastal Cordillera of northern Chile: Insights from zircon U-Pb dating and trace element geochemistry, Gondwana Res., 93, 48–72, https://doi.org/10.1016/j.gr.2021.01.007, 2021.

Juez-Larré, J., Kukowski, N., Dunai, T. J., Hartley, A. J., and Andriessen, P. A. M.: Thermal and exhumation history of the Coastal Cordillera arc of northern Chile revealed by thermochronological dating, Tectonophysics, 495, 48–66, https://doi.org/10.1016/j.tecto.2010.06.018, 2010.

Karger, D. N., Conrad, O., Böhner, J., Kawohl, T., Kreft, H., Soria-Auza, R. W., Zimmermann, N. E., Linder, H. P., and Kessler, M.: Climatologies at high resolution for the earth's land surface areas, Sci. Data, 4, 1–20, https://doi.org/10.1038/sdata.2017.122, 2017.

Koesuma, S., Ridwan, M., Nugraha, A. D., Widiyantoro, S., and Fukuda, Y.: Preliminary estimation of engineering bedrock depths from microtremor array measurements in Solo, Central Java, Indonesia, J. Math. Fundam. Sci., 49, 306–320, https://doi.org/10.5614/j.math.fund.sci.2017.49.3.8, 2017.

Krone, L. V, Hampl, F. J., Schwerdhelm, C., Bryce, C., Ganzert, L., Kitte, A., Übernickel, K., Dielforder, A., Aldaz, S., Oses-Pedraza, R., Perez, J. P. H., Sanchez-Alfaro, P., Wagner, D., Weckmann, U., and von Blanckenburg, F.: Deep weathering in the semi-arid Coastal Cordillera, Chile, Sci. Rep., 11, 1–15, https://doi.org/10.1038/s41598-021-90267-7, 2021.

Lehnert, L. W., Thies, B., Trachte, K., Achilles, S., Osses, P., Baumann, K., Schmidt, J., Samolov, E., Jung, P., Leinweber, P., Karsten, U., Büdel, B., and Bendix, J.: A case study on fog/low stratus occurrence at las lomitas, atacama desert (Chile) as a water source for biological soil crusts, Aerosol Air Qual. Res., 18, 254–269, https://doi.org/10.4209/aaqr.2017.01.0021, 2018.

Liu, X., Zhu, T., and Hayes, J.: Critical Zone Structure by Elastic Full Waveform Inversion of Seismic Refractions in a Sandstone Catchment, Central Pennsylvania, USA, J. Geophys. Res. Solid Earth, 127, 1–17,

https://doi.org/10.1029/2021JB023321, 2022.

Lodes, E., Scherler, D., Van Dongen, R., and Wittmann, H.: The story of a summit nucleus: Hillslope boulders and their effect on erosional patterns and landscape morphology 2 in the Chilean Coastal Cordillera, 305–324, 2023.

Maghami, S., Sohrabi-Bidar, A., Bignardi, S., Zarean, A., and Kamalian, M.: Extracting the shear wave velocity structure of deep alluviums of "Qom" Basin (Iran) employing HVSR inversion of microtremor recordings, J. Appl. Geophys., 185, 104246, https://doi.org/10.1016/j.jappgeo.2020.104246, 2021.

Mahajan, A. K., Mundepi, A. K., Chauhan, N., Jasrotia, A. S., Rai, N., and Gachhayat, T. K.: Active seismic and passive microtremor HVSR for assessing site effects in Jammu city, NW Himalaya, India-A case study, J. Appl. Geophys., 77, 51–62, https://doi.org/10.1016/j.jappgeo.2011.11.005, 2012.

Maksaev, V., Munizaga, F., and Tassinari, C.: Timing of the magmatism of the paleo-pacific border of Gondwana: U-Pb geochronology of Late Paleozoic to Early Mesozoic igneous rocks of the north Chilean Andes between 20° and 31°S, 447–506 pp., https://doi.org/10.5027/andgeoV41n3-a01, 2014.

Moon, S. W., Subramaniam, P., Zhang, Y., Vinoth, G., and Ku, T.: Bedrock depth evaluation using microtremor measurement: empirical guidelines at weathered granite formation in Singapore, J. Appl. Geophys., 171, 103866, https://doi.org/10.1016/j.jappgeo.2019.103866, 2019.

Nagamani, D., Sivaram, K., Rao, N. P., and Satyanarayana, H. V. S.: Ambient noise and earthquake HVSR modelling for site characterization in southern mainland, Gujarat, J. Earth Syst. Sci., 129, https://doi.org/10.1007/s12040-020-01443-8, 2020.

Nelson, S. and McBride, J.: Application of HVSR to estimating thickness of laterite weathering profiles in basalt, Earth Surf. Process. Landforms, 44, 1365–1376, https://doi.org/10.1002/esp.4580, 2019.

Oeser, R. A. and Von Blanckenburg, F.: Do degree and rate of silicate weathering depend on plant productivity?, Biogeosciences, 17, 4883–4917, https://doi.org/10.5194/bg-17-4883-2020, 2020.

Oeser, R. A., Stroncik, N., Moskwa, L. M., Bernhard, N., Schaller, M., Canessa, R., van den Brink, L., Köster, M., Brucker, E., Stock, S., Fuentes, J. P., Godoy, R., Matus, F. J., Oses Pedraza, R., Osses McIntyre, P., Paulino, L., Seguel, O., Bader, M. Y., Boy, J., Dippold, M. A., Ehlers, T. A., Kühn, P., Kuzyakov, Y., Leinweber, P., Scholten, T., Spielvogel, S., Spohn, M., Übernickel, K., Tielbörger, K., Wagner, D., and von Blanckenburg, F.: Chemistry and microbiology of the Critical Zone along a steep climate and vegetation gradient in the Chilean Coastal Cordillera, Catena, 170, 183–203, https://doi.org/10.1016/j.catena.2018.06.002, 2018.

Olona, J., Pulgar, J. A., Fernández-Viejo, G., López-Fernández, C., and González-Cortina, J. M.: Weathering variations in a granitic massif and related geotechnical properties through seismic and electrical resistivity methods, Near Surf. Geophys., 8, 585–599, https://doi.org/10.3997/1873-0604.2010043, 2010.

Parolai, S., Picozzi, M., Richwalski, S. M., and Milkereit, C.: Joint inversion of phase velocity dispersion and H/V ratio curves from seismic noise recordings using a genetic algorithm, considering higher modes, Geophys. Res. Lett., 32, 1–4, https://doi.org/10.1029/2004GL021115, 2005.

Pastén, C., Sáez, M., Ruiz, S., Leyton, F., Salomón, J., and Poli, P.: Deep characterization of the Santiago Basin using HVSR

https://doi.org/10.5194/egusphere-2023-1813
Preprint. Discussion started: 14 August 2023

and cross-correlation of ambient seismic noise, Eng. Geol., 201, 57–66, https://doi.org/10.1016/j.enggeo.2015.12.021, 2016.

Pilz, M., Parolai, S., Picozzi, M., Wang, R., Leyton, F., Campos, J., and Zschau, J.: Shear wave velocity model of the Santiago de Chile basin derived from ambient noise measurements: A comparison of proxies for seismic site conditions and amplification, Geophys. J. Int., 182, 355–367, https://doi.org/10.1111/j.1365-246X.2010.04613.x, 2010.

Piña-Flores, J., Cárdenas-Soto, M., García-Jerez, A., Seivane, H., Luzón, F., and Sánchez-Sesma, F. J.: Use of peaks and troughs in the horizontal-to-vertical spectral ratio of ambient noise for Rayleigh-wave dispersion curve picking, J. Appl. Geophys., 177, 104024, https://doi.org/10.1016/j.jappgeo.2020.104024, 2020.

Rodríguez, M. P., Charrier, R., Brichau, S., Carretier, S., Farías, M., Parseval, P., and Ketcham, R. A.: Latitudinal and Longitudinal Patterns of Exhumation in the Andes of North-Central Chile, Tectonics, 37, 2863–2886, https://doi.org/10.1029/2018TC004997, 2018.

Ryberg, T. and Haberland, C.: Bayesian simultaneous inversion for local earthquake hypocentres and 1-D velocity structure using minimum prior knowledge, Geophys. J. Int., 218, 840–854, https://doi.org/10.1093/gji/ggz177, 2019.

Sernageomin: Mapa Geológico de Chile. Servicio Nacional de Geología y Minería Santiago, 1982.

SESAME: Guidelines for The Implementation of The H/V Spectral Ratio Technique on Ambient Vibrations-Measurements, Processing and Interpretations, SESAME European Research Project, SESAME Site Eff. Assess. using Ambient Excit., 1–62, 2004.

Stannard, D., Meyers, J., and Dronfield, T.: Passive seismic horizontal to vertical spectral ratio (HVSR) surveying to help define bedrock depth, structure and layering in shallow coal basins, ASEG Ext. Abstr., 2019, 1–5, https://doi.org/10.1080/22020586.2019.12073175, 2019.

Stierman, D. J. and Healy, J. H.: A study of the depth of weathering and its relationship to the mechanical properties of near-surface rocks in the Mojave Desert, Pure Appl. Geophys. PAGEOPH, 122, 425–439, https://doi.org/10.1007/BF00874609, 1984.

Stroncik, N. and von Blanckenburg, F.: How does deep granite weather? Fractures matter but fracture size counts, 2022.

Trichandi, R., Bauer, K., Ryberg, T., Scherler, D., Bataille, K., and Krawczyk, C. M.: Combined seismic and borehole investigation of the deep granite weathering structure—Santa Gracia Reserve case in Chile, Earth Surf. Process. Landforms, 1–15, https://doi.org/10.1002/esp.5457, 2022.

Trichandi, R., Bauer, K., Ryberg, T., Wawerzinek, B., Araya Vargas, J., von Blanckenburg, F., and Krawczyk, C. M.: Shear-wave velocity imaging of weathered granite in La Campana (Chile) from Bayesian inversion of H/V spectral ratio data, J. Appl. Geophys., 2023.

Vantassel, J.: hvsrpy, https://doi.org/http://doi.org/10.5281/zenodo.3666956, 2020.

Vantassel, J.: jpvantassel/hvsrpy: v1.0.0, https://doi.org/10.5281/ZENODO.5563211, 2021.

Vázquez, M., Ramírez, S., Morata, D., Reich, M., Braun, J. J., and Carretier, S.: Regolith production and chemical weathering of granitic rocks in central Chile, Chem. Geol., 446, 87–98, https://doi.org/10.1016/j.chemgeo.2016.09.023, 2016.

Wathelet, M., Jongmans, D., and Ohrnberger, M.: Surface-wave inversion using a direct search algorithm and its application

https://doi.org/10.5194/egusphere-2023-1813
Preprint. Discussion started: 14 August 2023

to ambient vibration measurements, Near Surf. Geophys., 2, 211–221, https://doi.org/10.3997/1873-0604.2004018, 2004.

Wathelet, M., Chatelain, J. L., Cornou, C., Giulio, G. Di, Guillier, B., Ohrnberger, M., and Savvaidis, A.: Geopsy: A user-
545 friendly open-source tool set for ambient vibration processing, Seismol. Res. Lett., https://doi.org/10.1785/0220190360, 2020.

a

https://doi.org/10.5194/egusphere-2023-1813
Preprint. Discussion started: 14 August 2023

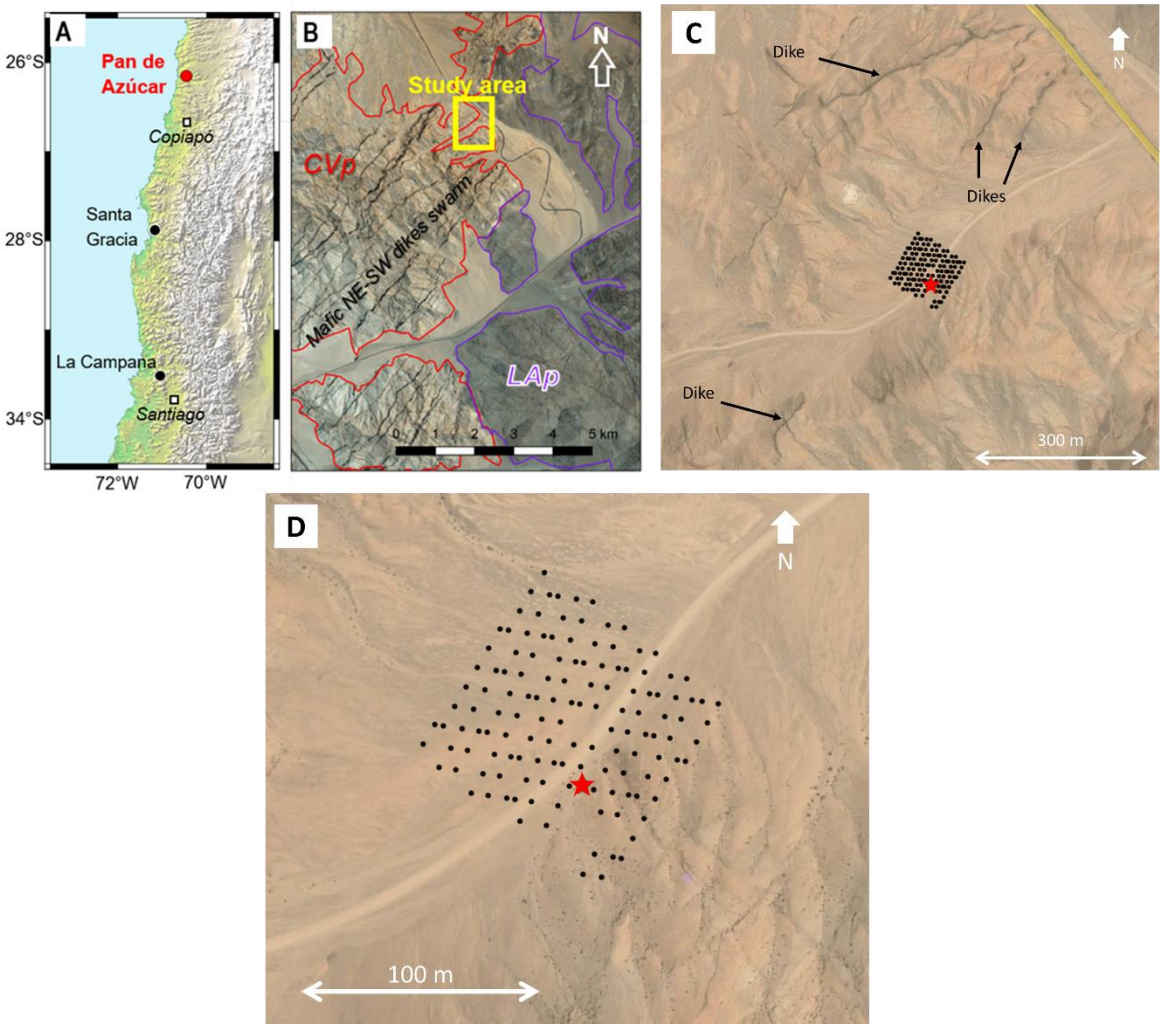

550 **Figure 1. Site information of the Chile Pan de Azúcar study site: (A) Study site location. (B) Local geology information of the study area (Sernageomin, 1982). Red and purple lines outline the Cerros del Vetado (CVp) and Las Ánimas (LAp) plutons, respectively (modified from Godoy & Lara, 1998). (C) Google Earth image of the study site (© Google Earth 2019). Some of the mafic dikes outcropping in the area are highlighted. (D) Seismic array. Red dots in (C) and (D) show the position of seismic sensors. The red star shows the location of the borehole (WGS 84 coordinates 26.30272° S, 70.45735° W).**

555

https://doi.org/10.5194/egusphere-2023-1813
Preprint. Discussion started: 14 August 2023

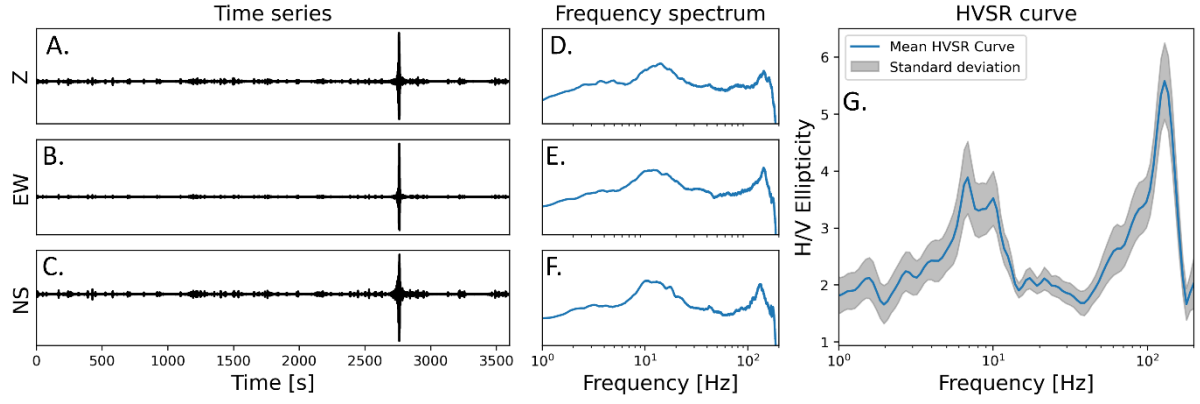

Figure 2. Steps of HVSR curve extraction from the (A–C) 60 minutes 3 components seismic noise recordings, (D-F) the respective frequency spectrum, and (G) the resulting HVSR curve extracted using the hvsrpy package (Vantassel, 2020).

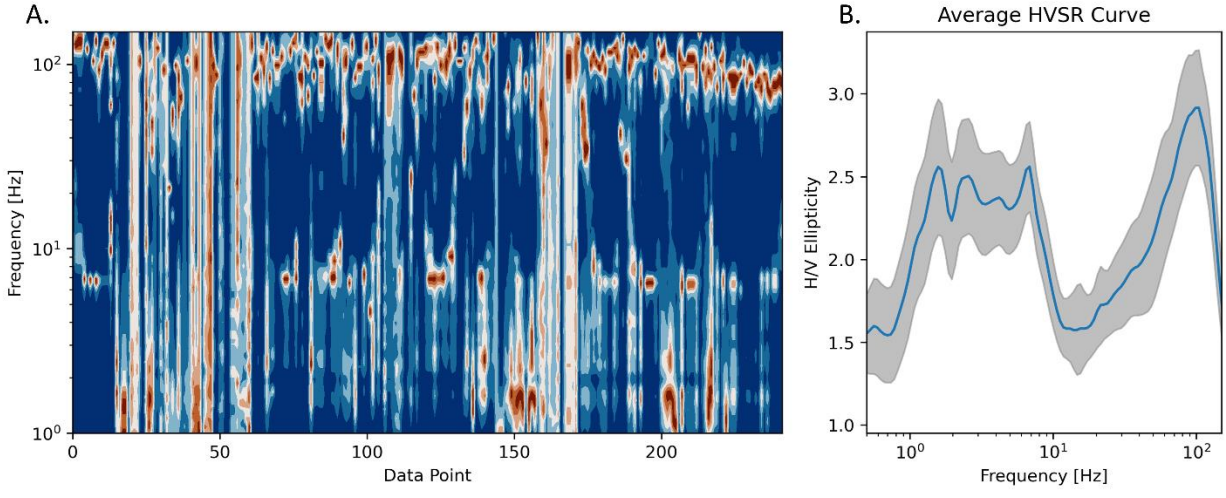

Figure 3. Collection of the extracted HVSR curve in the survey area (A) and the mean HVSR curve (B).

https://doi.org/10.5194/egusphere-2023-1813
Preprint. Discussion started: 14 August 2023

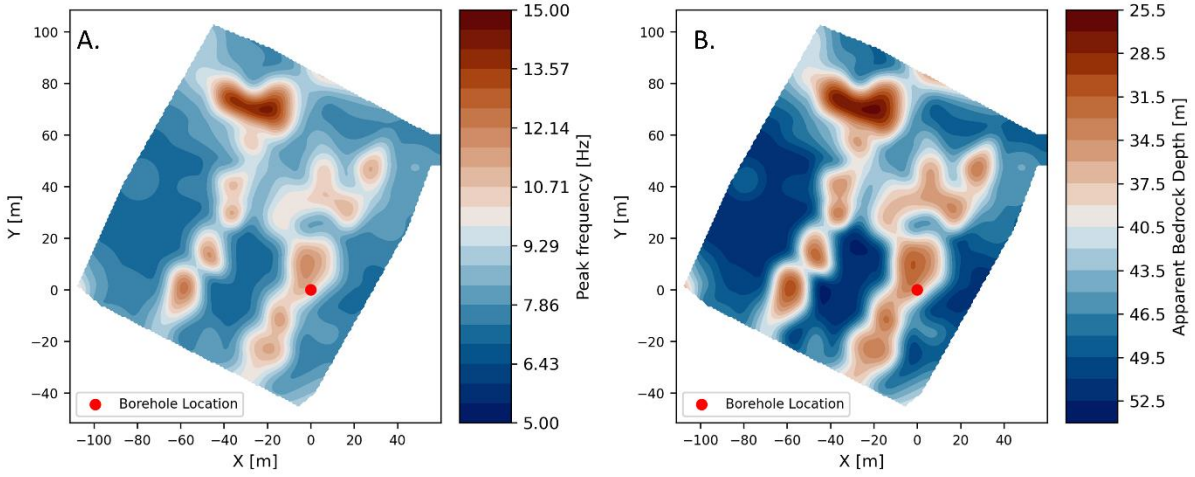

565 **Figure 4 Resulting (A) peak frequency and (B) apparent fresh bedrock depth map assuming Vs = 1.50 km/s. The red dot represents the borehole location. Higher frequency in (A) is related to a shallower bedrock, while inversely, lower frequency is connected to a deeper bedrock**

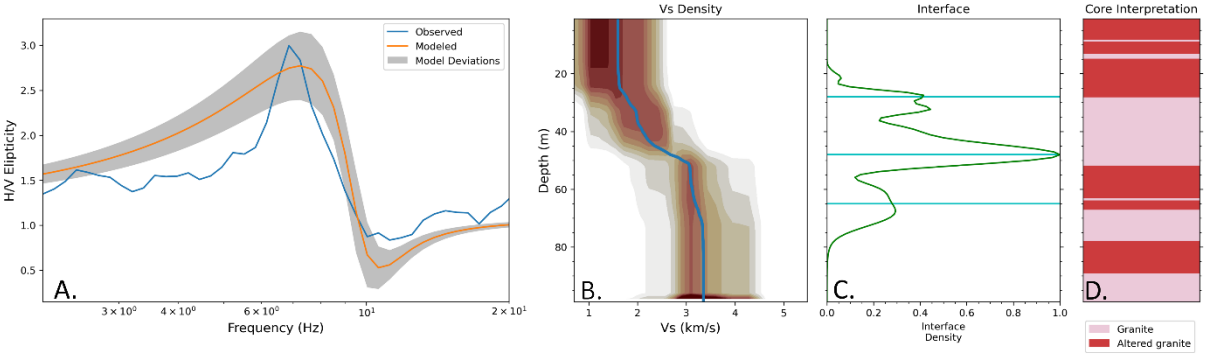

570 **Figure 5. Bayesian inversion result of the HVSR curve from the data points closest to the borehole location: (A) observed and modeled HVSR curve, (B) 1D Vs probability density from all the inversion chain and the mean Vs profile, (C) interface probability function, and (D) interpretation from the borehole coring modified from Stroncik & von Blanckenburg (2022).**

https://doi.org/10.5194/egusphere-2023-1813
Preprint. Discussion started: 14 August 2023

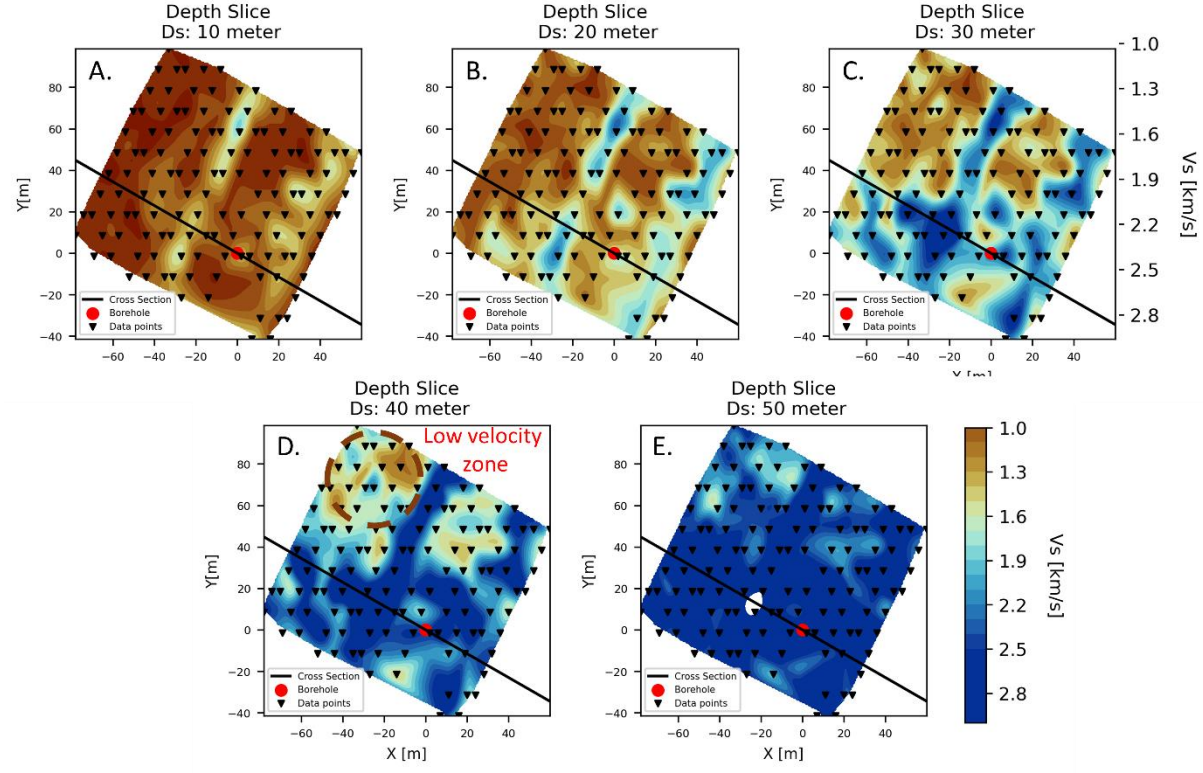

575 **Figure 6 Depth slice of the pseudo-3D Vs model produced from the inversion of HVSR curves. From (A) to (E) are depth slices with steps of 10 meters from the surface. The inverted black triangles are the geophone location and the black line represents a NW-SE cross-section that goes through the borehole location of the red dot.**

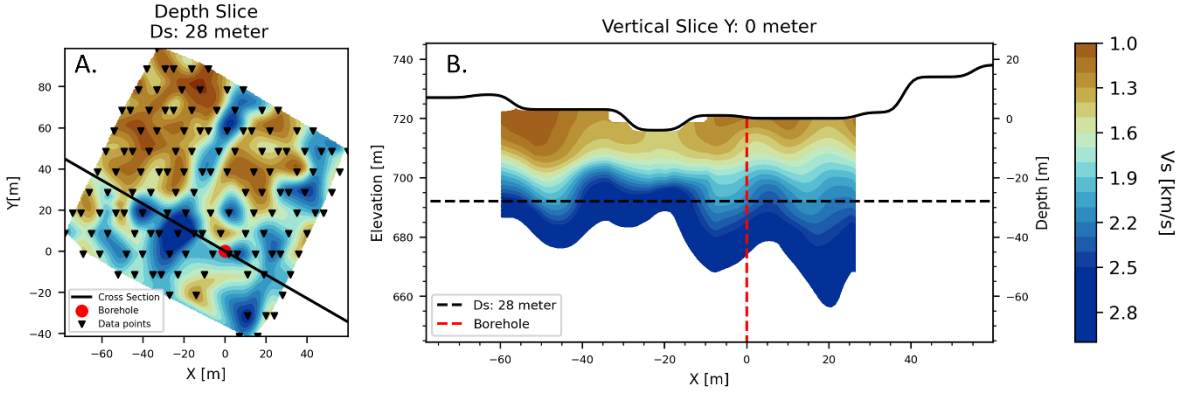

580 **Figure 7. Vs model of the study area: (A) horizontal depth slice at 28-meter depth, and (B) vertical slice from the cross-section line in (A). The dashed black line in (B) represents the selected 28-meter depth line, and the dashed red line represents the borehole location.**

https://doi.org/10.5194/egusphere-2023-1813
Preprint. Discussion started: 14 August 2023

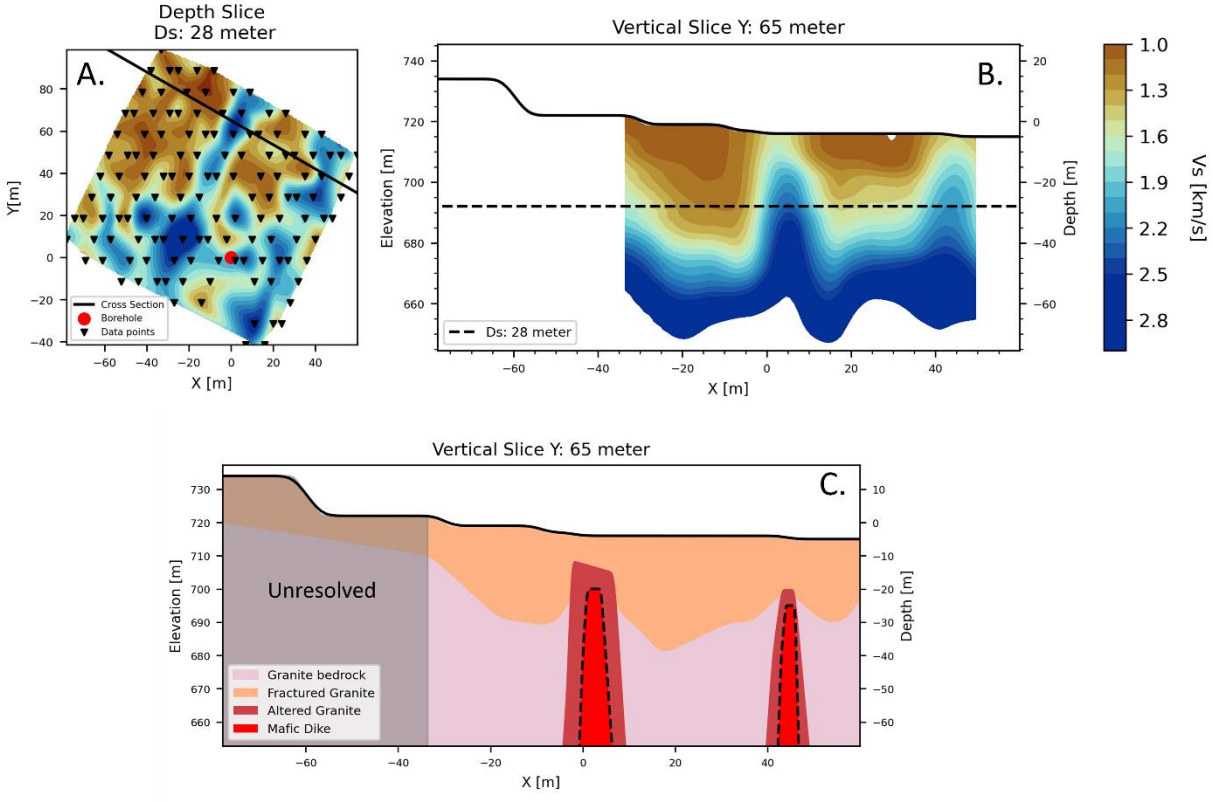

585 **Figure 8. Vs model of the study area: (A) horizontal depth slice at 28-meter depth, (B) vertical slice from the cross-section line in (A), and (C) conceptual model of the cross-section in (B). The red dot in (A) is the borehole location, and the inverted triangles are the geophone location. The dashed black line in (B) represents the selected 28-meter depth line.**